


## Dependence of spin pumping in W/CoFeB heterostructures on the structural phase of tungsten

Deepika Jhahria,<sup>1</sup> Nilamani Behera,<sup>2</sup> Dinesh K. Pandya,<sup>1</sup> and Sujeet Chaudhary<sup>1,\*</sup>

<sup>1</sup>*Thin Film Laboratory, Department of Physics, Indian Institute of Technology Delhi, New Delhi 110016, India*

<sup>2</sup>*Department of Engineering Sciences, Uppsala University, Box 534, SE-751 21 Uppsala, Sweden*

 (Received 19 September 2018; revised manuscript received 14 December 2018; published 24 January 2019)

We report the systematic dependence of spin pumping in tungsten (W)/CoFeB heterostructures on the structural phase of W, which is intricately related to argon gas pressure ( $p_{Ar}$ ) maintained during the sputter deposition. We found that with increasing  $p_{Ar}$  the structural phase of W changes from mixed ( $\alpha + \beta$ ) phase to pure  $\beta$  phase. The  $\beta$ -W is stabilized in films for the high thickness of 40 nm which is desirable for spin devices. Using ferromagnetic resonance measurement of W( $p_{Ar}$ )/CoFeB heterostructures, it is shown that enhancement of magnetic damping ( $\alpha_{eff}$ ) from spin pumping is more in  $\beta$ -W compared to ( $\alpha + \beta$ )-W. The effective spin mixing conductance ( $g_{eff}^{\uparrow\downarrow}$ ) is estimated for different phases of W from the linear evolution of  $\alpha_{eff}$  with the inverse thickness of the CoFeB layer. For  $\beta$ -W, the  $g_{eff}^{\uparrow\downarrow}$  is found to be larger than that of ( $\alpha + \beta$ )-W and it is attributed to different interface structure. Thus, effective tuning of spin pumping efficiency can be achieved using different W crystal phases. We also studied the dependence of  $\alpha_{eff}$  on  $\beta$ -W film thickness to calculate the value of spin-diffusion length ( $\lambda_{SD}$ ) and intrinsic spin mixing conductance ( $g_{\beta-W}^{\uparrow\downarrow}$ ) using both the ballistic and diffusive spin transport models.

DOI: [10.1103/PhysRevB.99.014430](https://doi.org/10.1103/PhysRevB.99.014430)

### I. INTRODUCTION

The efficient generation, manipulation, and detection of spin current are of foremost importance for the development of spin based magnetic data storage and spin logic devices [1,2]. The spin Hall effect (SHE) [3,4], spin pumping [5–8], and spin Seebeck effect [9,10] constitute some of the possible routes that have been used to generate pure spin current. Spin pumping is a widely accepted method of spin injection into normal metal (NM), as no microfabrication is required for the device structure. In spin pumping based devices, the magnetization precession of the ferromagnetic (FM) layer injects spin current into the adjacent NM layer. The spin mixing conductance ( $g^{\uparrow\downarrow}$ ) and spin-diffusion length ( $\lambda_{SD}$ ) are two important characteristic parameters of spin pumping which decide whether the dynamically pumped spin current in the NM layer will dissipate or return back to the FM layer [2,5,11,12]. The dissipation of spin current into the NM layer is accompanied by loss of angular momentum in the FM layer which leads to enhancement in the effective Gilbert damping constant ( $\alpha_{eff}$ ) of the FM layer [13]. Thus, spin pumping allows the possible control of magnetization dynamics, which is crucial in several spintronic devices such as spin transfer torque magnetic random-access memory (MRAM), spin torque nano-oscillators, etc. [14–16]. The enhanced damping is more prominent in metals with high spin-orbit coupling (SOC) because of stronger interaction between electron spin and lattice.

Tungsten (W) in its  $\beta$  phase (A-15 structure) is attracting great interest, as it exhibits giant spin Hall effect due to large SOC [17–20]. Very high spin Hall angle (SHA, a measure of

the efficiency of charge to spin current conversion) is reported for  $\beta$ -W (up to 0.5 [21]) compared to other transition-metal elements such as Pt (0.08) [22–24] and  $\beta$ -Ta (0.15) [25]. Thus, large SHE induced spin-orbit torque can be generated, which is of interest for magnetization switching [25,26], excitation of precessional magnetization dynamics [27,28], and domain-wall motion [29,30]. However, there exists another crystalline state of W, namely, the  $\alpha$ -W (bcc structure). It is known that the fabrication of phase pure  $\beta$ -W thin films to higher thicknesses and without adding oxygen in the growth chamber is particularly challenging [19,20,31–35]. In contrast to  $\beta$ -W, very small SHA is reported for the  $\alpha$  phase ( $<0.07$ ) and mixed ( $\alpha + \beta$ ) phase (0.18) of W [17,36]. The SHA and spin mixing conductance have been found to be correlated [37]. Consequently, one would expect that spin pumping might also be significantly dependent on structural phase changes in W thin films, which has not been yet experimentally studied. Furthermore, the magnitude of spin-orbit torque is dependent on the efficiency of spin current transmission across the FM/NM interface, governed by spin pumping parameter  $g^{\uparrow\downarrow}$ , which remains undefined for various W crystal phases. Therefore, a detailed understanding of the formation of  $\beta$ -W as well as the dependence of spin pumping on different phases of W is crucial from both fundamental and technological viewpoints.

Here, we report the correlation of structural phase changes in W thin films with spin pumping efficiency in W/CoFeB heterostructures. The W crystalline state is controlled by varying the argon gas pressure ( $p_{Ar}$ ) during sputtering, and it is found that with increasing  $p_{Ar}$  the structural phase of W eventually changes from mixed ( $\alpha + \beta$ ) to pure  $\beta$  phase. The  $\beta$ -W is stabilized in films having a thickness of  $\approx 40$  nm. The ferromagnetic resonance (FMR) technique is used to measure the spin pumping induced damping enhancement in W( $p_{Ar}$ )/CoFeB heterostructures. We found that  $\beta$ -W gives

\*Corresponding author: [sujeetc@physics.iitd.ac.in](mailto:sujeetc@physics.iitd.ac.in)

rise to greater enhancement in damping and higher effective spin mixing conductance ( $g_{\text{eff}}^{\uparrow\downarrow}$ ) compared to  $(\alpha + \beta)$ -W. We also determined the intrinsic spin mixing conductance ( $g_{\beta\text{-W}}^{\uparrow\downarrow}$ ) for the  $\beta$ -W/CoFeB interface and the spin-diffusion length ( $\lambda_{\text{SD}}$ ) of  $\beta$ -W by studying the dependence of  $\alpha_{\text{eff}}$  on  $\beta$ -W thickness. These basic properties of W are beneficial for a complete understanding of this high SOC material, which is of interest for pure spin current based devices.

## II. EXPERIMENTAL DETAILS

Thin films of W(40 nm) were deposited at room temperature on naturally oxidized Si substrates using a pulsed-dc magnetron sputtering system (Excel Instruments, India) equipped with a cryopump achieving base pressure better than  $2 \times 10^{-7}$  Torr. The confocal sputtering guns have a diameter of 5 cm and the target to substrate distance is kept at 11 cm. The deposition of W films was carried out at different values of argon gas working pressure ( $p_{\text{Ar}}$ ) while maintaining a constant low sputtering power of 12 W to the W target (99.99% pure). The  $p_{\text{Ar}}$  was systematically varied from 3 to 20 mTorr. The deposition rate of W at various  $p_{\text{Ar}}$  was calibrated using x-ray reflectivity (XRR) measurements and subsequently the deposition time for W ( $p_{\text{Ar}}$ ) films was appropriately chosen to deposit W films having a desired constant thickness. The growth rates ( $R$ ) were found to increase from  $0.0080(\pm 0.0002)$  nm/s for  $p_{\text{Ar}} = 3$  mTorr to  $0.0105(\pm 0.0002)$  nm/s for  $p_{\text{Ar}} = 15$  mTorr and then decrease slightly to  $0.0100(\pm 0.0002)$  nm/s for  $p_{\text{Ar}} = 20$  mTorr. The crystallographic structure of W films was studied using an X<sup>3</sup>pert pro x-ray diffractometer equipped with a Cu-K $\alpha$  (1.54 Å) source. The resistivity of films was measured using four-point probe method.

For spin pumping studies, we prepared a layered structure of Si/W(10 nm,  $p_{\text{Ar}}$ )/Co<sub>60</sub>Fe<sub>20</sub>B<sub>20</sub>(15 nm)/Ta(2 nm). The CoFeB films exhibited in-plane uniaxial magnetic anisotropy, induced as a consequence of oblique sputtering, with the easy axis (EA) along the incident direction [38]. A 2-nm-thin capping layer of Ta was used to prevent the oxidation of CoFeB from the atmosphere. Since the thicknesses of both CoFeB and W are held constant, we have labeled the bilayers as W( $p_{\text{Ar}}$ )/CoFeB. The density, thickness, and interface roughness of individual layers in W( $p_{\text{Ar}}$ )/CoFeB heterostructures were accurately determined by XRR measurement. Two additional sets of sample series were also sputter deposited: (1) Si/W(10 nm,  $p_{\text{Ar}}$ )/Co<sub>60</sub>Fe<sub>20</sub>B<sub>20</sub>( $t_{\text{CoFeB}}$ )/Ta(2 nm) thin films with variable CoFeB thickness ( $t_{\text{CoFeB}} = 5, 10, 15, \text{ and } 25$  nm) for  $p_{\text{Ar}} = 3$  and 10 mTorr; (2) Si/W( $t_{\text{W}}$ ,  $p_{\text{Ar}} = 10$  mTorr)/Co<sub>60</sub>Fe<sub>20</sub>B<sub>20</sub>(15 nm)/Ta(2 nm) thin films with variable W thickness ( $t_{\text{W}} = 1, 2, 3, 4, 6, 8, 10, 12, 16, 20, \text{ and } 25$  nm). From the first set of samples the effective spin mixing conductance ( $g_{\text{eff}}^{\uparrow\downarrow}$ ) is deduced, and from the second set the intrinsic spin mixing conductance ( $g_{\text{W}}^{\uparrow\downarrow}$ ) of the W/CoFeB interface and the spin-diffusion length ( $\lambda_{\text{SD}}$ ) of W are determined. Additionally, to evaluate the Gilbert damping of single layer CoFeB, a reference sample Si/Co<sub>60</sub>Fe<sub>20</sub>B<sub>20</sub>(15 nm)/Ta(2nm), labeled as W(0)/CoFeB, was also grown under similar conditions.

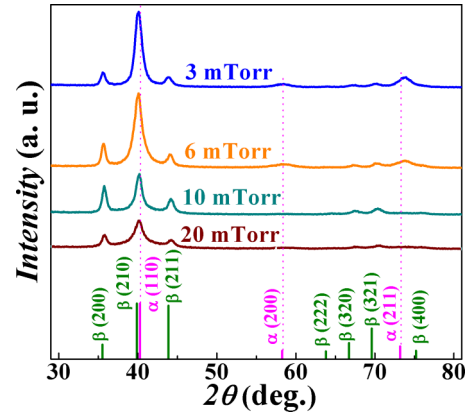


FIG. 1. The XRD patterns for W(40 nm) films deposited at different  $p_{\text{Ar}}$ . The Bragg peak positions corresponding to reference data (extracted from the JCPDS database) of  $\alpha$  (bcc) and  $\beta$  (A15) phase of tungsten together with their relative peak intensity are shown as vertical bars in the bottom. The dotted lines are used to extend the vertical bars to pass through peaks corresponding to  $\alpha$  phase.

We used vibrating sample magnetometer (VSM) option in a Quantum Design physical property measurement system (model: Evercool II) to measure the saturation magnetization of the films. The magnetization dynamics of the films was characterized using the broadband (5–12 GHz) in-plane FMR technique employing a vector network analyzer and coplanar waveguide (CPW) based transmission line. Here, the samples (with the film side facing the CPW) are subjected to field sweep through resonance at different values of constant microwave frequencies. The signal to noise ratio is improved using a combination of field modulation and lock-in detection. The external static magnetic field is modulated at 211.5 Hz by a very small alternating magnetic field of 1.3 Oe provided by a pair of Helmholtz coils. Thus, the measured FMR spectrum is proportional to the field derivative of absorbed microwave power. Subsequently, the values of the resonance field ( $H_r$ ) and field linewidth ( $\Delta H$ ) were determined by fitting of the extracted FMR spectra with the derivative of the Lorentzian function.

## III. RESULTS AND DISCUSSION

Figure 1 shows the glancing angle ( $1^\circ$ ) XRD pattern for W(40 nm) films deposited at different  $p_{\text{Ar}}$ . All the observed peaks in the XRD pattern of W ( $p_{\text{Ar}}$ ) films can be matched with the reference data of either bcc or A15 structure of W extracted from the joint committee on powder diffraction system (JCPDS) file data [references 04-0806 ( $\alpha$ -W) and 47-1319 ( $\beta$ -W)] depicted at the bottom of the figure with peak labels. The W films grown at lower  $p_{\text{Ar}}$  ( $\leq 6$  mTorr) are highly crystalline and composed primarily of  $\alpha$  phase with some mixed  $\beta$  phase as is evident from the dominant presence of (110) and (211) reflection peaks of the bcc structure. On the other hand, for  $p_{\text{Ar}} \geq 10$  mTorr, a single phase  $\beta$ -W is obtained with the absence of (110), (200), and (211) reflection peaks of the  $\alpha$  phase. The metastable  $\beta$  phase in films exists up to  $p_{\text{Ar}} = 20$  mTorr. Observing  $\beta$ -W at such high thickness

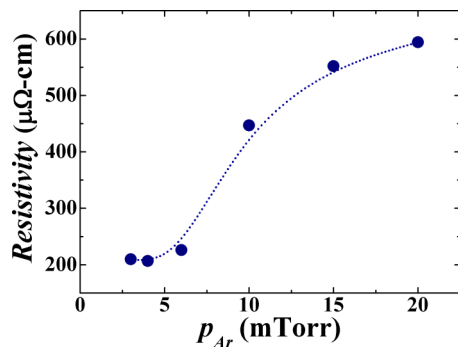


FIG. 2. The resistivity of W(40 nm) films as a function of  $p_{Ar}$ . The dotted line is a guide to the eyes.

of 40 nm is certainly advantageous in the present scenario as W generally exhibits thickness dependent structural transition [17,20,31,34–36]. Since annealing is required during most device fabrications, it is of interest to see the thermal stability of the films. We found that after thermal annealing of 40-nm films at 300 °C for 1 h the  $(\alpha + \beta)$ -W films transform into pure  $\alpha$  phase, whereas the  $\beta$ -W films transform into mixed  $(\alpha + \beta)$  phase only, and not into pure  $\alpha$  phase even on annealing at 350 °C (data not shown).

The average lattice constants calculated from  $\alpha$  (211) and  $\beta$  (200) peaks were found to remain constant as a function of  $p_{Ar}$  with values of 0.317 nm (bcc) and 0.504 nm (A-15) which match very well with the literature bulk values of 0.3165 and 0.504 nm, respectively [32]. The average sizes of  $\alpha$ -W and  $\beta$ -W crystallites were also estimated from  $\alpha$  (211) and  $\beta$  (200) peaks using Scherrer's formula and were found to remain unchanged, with values  $\approx 8$  nm for  $\alpha$ -W and  $\approx 15$  nm for  $\beta$ -W, for the entire pressure range [39].

To further verify the phase changes in W thin films with  $p_{Ar}$ , the electron transport study is done using the resistivity measurement. It is known that the formation of  $\beta$ -W films is characterized by very large resistance, since the A-15 structure is associated with strong electron-phonon scattering while the  $\alpha$ -W exhibit fairly low resistivity [17,31,33,34]. Figure 2 shows the resistivity of W films as a function of  $p_{Ar}$ . It can be seen that the resistivity of W thin films does not change significantly for  $p_{Ar} \leq 6$  mTorr and is around 200  $\mu\Omega$  cm. Afterwards, there is a sharp rise in resistivity for  $p_{Ar} > 6$  mTorr with a value of  $\approx 450$   $\mu\Omega$  cm at

$p_{Ar} = 10$  mTorr, and it continues to increase with increasing  $p_{Ar}$ , reaching up to  $\approx 600$   $\mu\Omega$  cm for  $p_{Ar} = 20$  mTorr. This observed higher resistivity for  $p_{Ar} > 6$  mTorr indicates the transformation of films into  $\beta$  phase and the values agree well with the previously reported resistivity values for  $\beta$ -W [40]. Thus, the resistivity results corroborate well with those of XRD measurement, which also suggests clear single phase formation of  $\beta$ -W for  $p_{Ar} = 10$ –20 mTorr while the  $(\alpha + \beta)$ -W with dominant of  $\alpha$  phase deposited in the low-pressure regime has much smaller resistivity than  $\beta$ -W.

Figure 3(a) shows the measured XRR spectra with their corresponding simulated curves for selected W( $p_{Ar}$ )/CoFeB thin films. At lower  $p_{Ar}$ , the XRR spectra exhibit well-defined oscillations for up to  $3^\circ$  indicating uniform deposition thickness and a smoother interface, while for higher  $p_{Ar}$  there is clear attenuation in oscillation at higher angles pointing to slightly higher W surface roughness. The simulated parameters, average mass density ( $D$ ), and rms surface roughness of the W layer are plotted as a function of  $p_{Ar}$  in Fig. 3(b). It can be seen that density of W films reduces with increase in  $p_{Ar}$  from close to the bulk value of  $\approx 18.2$  g/cm<sup>3</sup> ( $p_{Ar} = 3$  mTorr) to  $\approx 12.3$  g/cm<sup>3</sup> ( $p_{Ar} = 20$  mTorr) and this points to the formation of porous W films at higher  $p_{Ar}$ . In contrast, rms surface roughness of W increases from  $\approx 0.3$  to  $\approx 1.2$  nm as  $p_{Ar}$  increases from 3 to 20 mTorr. It is known that film growth kinetics is controlled by the mobility of sputtered adatoms on the substrate surface [41,42]. For deposition at higher  $p_{Ar}$ , the mobility of W atoms at the substrate can be significantly reduced due to numerous collisions and deflection with argon atoms and is not sufficient to allow migration of W atoms to preferred sites for a good crystalline growth, resulting in slightly rough and porous films. On the other hand, for lower  $p_{Ar}$ , the high mobility of sputtered W atoms is sufficient to overcome the surface diffusion energy, which results in stable crystalline growth and smoother films with a density close to bulk crystalline value.

The growth kinetics of W films can further help in understanding the stabilization of  $\beta$ -W at higher  $p_{Ar}$ . The metastable  $\beta$ -W is normally known to be stabilized by incorporation of some oxygen [21,32]. Since the W( $p_{Ar}$ ) films are grown under the same base pressure, the residual oxygen content in the chamber is the same for all the films. However, the increased porosity at higher  $p_{Ar}$  can enhance the exchange of oxygen incorporation, thereby stabilizing the A15 structure (in line with XRD measurement). Also, the

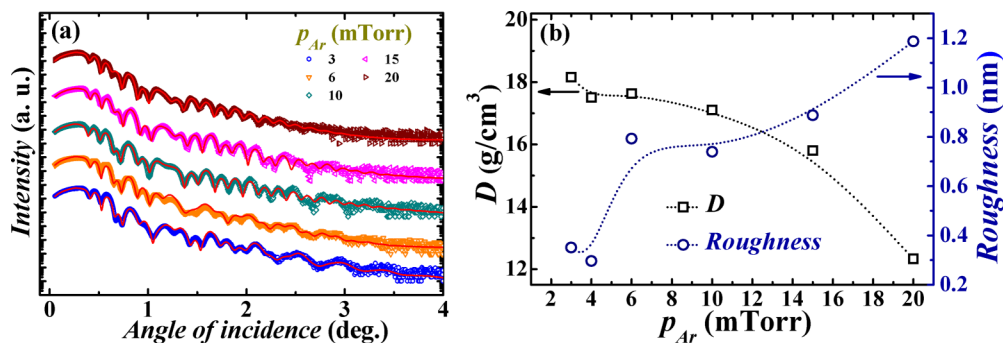


FIG. 3. (a) XRR spectra of the W( $p_{Ar}$ )/CoFeB films grown at various  $p_{Ar}$ . (b) The simulation parameter, average mass density ( $D$ ), and rms surface roughness of the W layer as a function of  $p_{Ar}$ . The dotted lines are guides to the eyes.

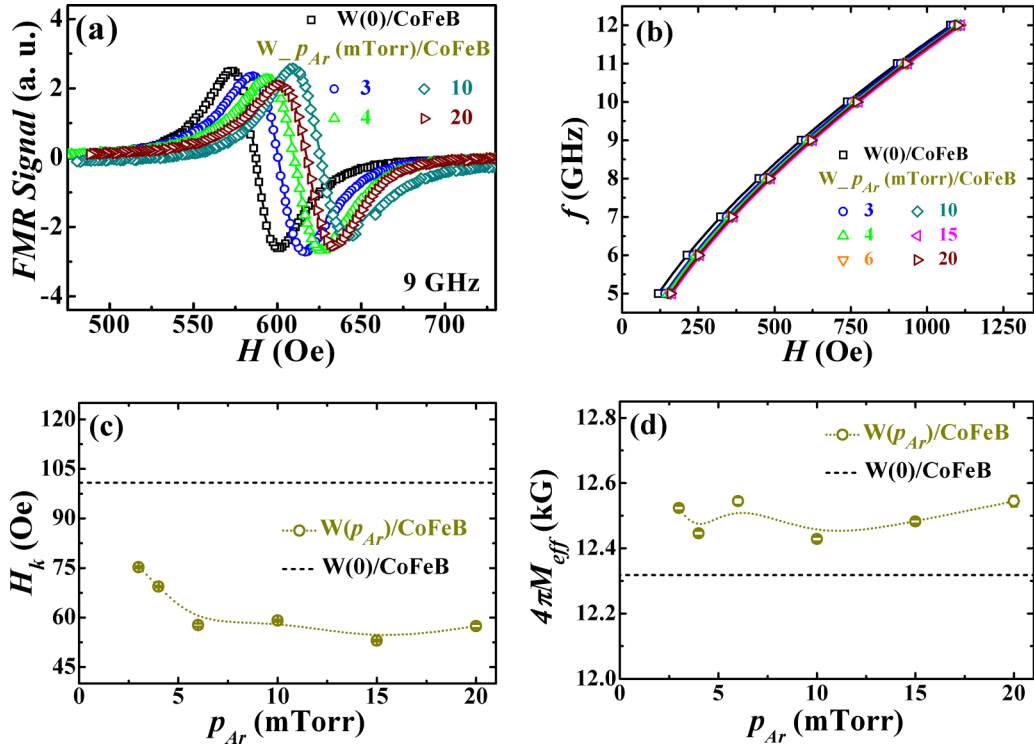


FIG. 4. (a) Field-swept normalized in-plane FMR spectra of the W(0)/CoFeB and W( $p_{Ar}$ )/CoFeB thin films recorded at 9 GHz. Open symbols and solid lines represent the experimental data and fits to the derivative of the Lorentzian function, respectively. (b) Variation of  $f$  vs  $H_r$ . Open symbols and solid lines represent the experimental data and fits to Eq. (1) respectively. (c) Dependence of  $H_k$  on  $p_{Ar}$ . (d) Variation of  $4\pi M_{eff}$  with  $p_{Ar}$ . The curved dotted lines are guides to the eyes.

numerous collisions at higher  $p_{Ar}$  might lead to a decrease in the deposition flux of W atoms reaching the substrate. The flux ( $F$ ) is calculated as  $F = R \frac{D}{m_w}$ , where  $m_w$  is the mass of a W atom. The  $F$  was found to increase from  $\approx 0.48 \text{ nm}^{-2} \text{ s}^{-1}$  for  $p_{Ar} = 3 \text{ mTorr}$  to  $\approx 0.56 \text{ nm}^{-2} \text{ s}^{-1}$  for  $p_{Ar} = 10 \text{ mTorr}$  and then drops in the 10–20-mTorr range to  $\approx 0.40 \text{ nm}^{-2} \text{ s}^{-1}$  for  $p_{Ar} = 20 \text{ mTorr}$ . Due to the lower deposition flux observed at higher  $p_{Ar}$ , the probability of incorporation of residual oxygen in the growing W films is higher, which leads to  $\beta$ -W stabilization [32,41].

For studying the systematic dependence of spin pumping on the structural phase of W, the in-plane FMR spectra of W( $p_{Ar}$ )/CoFeB films were recorded along the EA of CoFeB films over the frequency ( $f$ ) range of 5–12 GHz. For the purpose of comparison, the normalized FMR spectra of W(0)/CoFeB and W( $p_{Ar}$ )/CoFeB thin films recorded at 9 GHz are shown in Fig. 4(a). The observed change in resonance field ( $H_r$ ) is caused by anisotropy and magnetization variation in films. To extract the anisotropy field ( $H_k$ ) and effective magnetization ( $4\pi M_{eff}$ ), the  $f$  versus  $H_r$  plots [see Fig. 4(b)] were fitted using the Kittel equation [43]:

$$f = \frac{g\mu_B}{h} \sqrt{(H_r + H_k)(H_r + H_k + 4\pi M_{eff})}. \quad (1)$$

Here,  $h$  is Planck's constant,  $\mu_B$  is the Bohr magneton, and  $g$  ( $=2.15$ ) is the Landé  $g$  factor. Figure 4(c) presents the variation of  $H_k$  with  $p_{Ar}$  from which a slight decrease in  $H_k$  at higher  $p_{Ar}$  is clearly evident. This observed small reduction in

$H_k$  possibly arises from changes in interfacial microstructure and orbital moment in the films owing to the presence of different W phases [44]. Also, the W(0)/CoFeB film exhibits higher  $H_k$  than that with the W seed layer. Since the main aim of this paper is to analyze the magnetic damping and spin pumping efficiency, the identification of the anisotropy mechanism and its variation as a function of  $p_{Ar}$  is not considered here. The dependence of  $4\pi M_{eff}$  for W( $p_{Ar}$ )/CoFeB films on  $p_{Ar}$  is shown in Fig. 4(d). The  $4\pi M_{eff}$  values do not clearly depend on  $p_{Ar}$  with a mean value of  $\approx 12.5(\pm 0.5) \text{ kOe}$ . The values are higher compared to that of W(0)/CoFeB thin film, which indicates the W seed layer effect in terms of modifying the surface magnetism and magnetic anisotropy of the CoFeB layer [44,45]. The saturation magnetization ( $4\pi M_s$ ) values estimated using VSM are found to be very close to  $4\pi M_{eff}$  values.

The damping constant and related mechanism can be determined by analyzing the FMR linewidth ( $\Delta H$ ) at different frequencies. The frequency dependence of linewidth can mainly have two possible contributions: (1) the intrinsic Gilbert damping contribution, which is linear in frequency [46,47], and (2) the extrinsic two-magnon scattering (TMS) contribution, which leads to a nonlinear variation of linewidth with frequency [48,49]. Figure 5(a) shows  $\Delta H$  versus  $f$  plots of W(0)/CoFeB and W( $p_{Ar}$ )/CoFeB thin films. The linear behavior of  $\Delta H$  with frequency for all samples indicates that damping is predominantly governed by an intrinsic mechanism via electron-magnon scattering and the possible contribution from TMS can be ignored. Thus, the

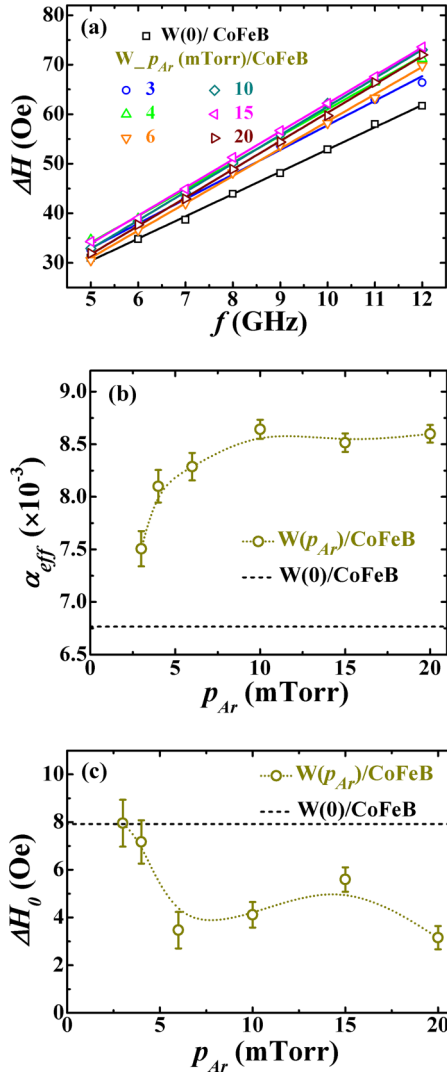


FIG. 5. (a) Variation of  $\Delta H$  vs  $f$  for W(0)/CoFeB and W( $p_{Ar}$ )/CoFeB thin films with open symbols and solid lines representing the experimental data and fits to Eq. (2), respectively. (b) Dependence of  $\alpha_{eff}$  on  $p_{Ar}$ . (c) Variation of  $\Delta H_0$  as a function of  $p_{Ar}$ . The curved dotted lines are guides to the eyes.

frequency dependence of  $\Delta H$  in films is expected to follow the relation [50]

$$\Delta H = \frac{2h\alpha_{eff}}{g\mu_B} f + \Delta H_0. \quad (2)$$

Here, the first term  $\frac{2h\alpha_{eff}}{g\mu_B} f$  corresponds to intrinsic linewidth contribution and is proportional to the effective Gilbert damping constant,  $\alpha_{eff}$ . The second term  $\Delta H_0$  describes an inhomogeneous line broadening caused by sample imperfections and is independent of frequency. The obtained  $\alpha_{eff}$  from the fit of experimental data is shown in Fig. 5(b) and it reveals that  $\alpha_{eff}$  values are significantly higher for W( $p_{Ar}$ )/CoFeB heterostructures compared to W(0)/CoFeB films. In terms of intrinsic origin, this enhanced damping in W( $p_{Ar}$ )/CoFeB films is attributed to the spin pumping mechanism caused by the W seed layer. There is a clear trend that  $\alpha_{eff}$  rapidly rises as  $p_{Ar}$  increases and peaks around  $p_{Ar} = 10$  mTorr. Thereafter, the  $\alpha_{eff}$  stays almost

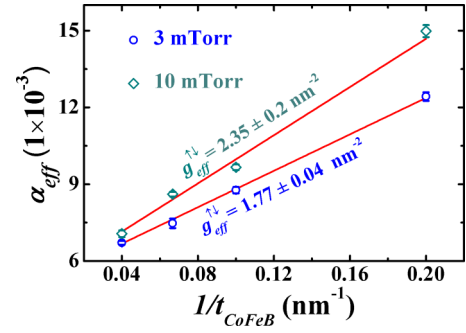


FIG. 6.  $\alpha_{eff}$  as a function of  $1/t_{CoFeB}$  for W(10 nm,  $p_{Ar}$ )/CoFeB( $t_{CoFeB}$ ) heterostructures with  $p_{Ar} = 3$  and 10 mTorr.

constant for  $p_{Ar}$  between 10 and 20 mTorr corresponding to W films with pure  $\beta$  phase only. The variation in damping correlates well with  $p_{Ar}$  dependent structural phase transition in W from ( $\alpha + \beta$ ) to  $\beta$  phase occurring at  $p_{Ar} = 10$  mTorr. This dependence of spin pumping on crystal structure of W films might indicate different values of spin mixing conductance for different W structural phases that we will present in the later sections. It is unlikely that the observed  $\alpha_{eff}(p_{Ar})$  trend may arise from the W( $p_{Ar}$ ) roughness variation, as an increase of roughness in the range  $p_{Ar} = 10$ –20 mTorr could not account for the almost constant damping. We should mention that the presence of magnetic anisotropy in films can also influence the damping [38,51]. However, the observed opposite trend of  $H_k$  [see Fig. 4(c)] compared to  $\alpha_{eff}$  with  $p_{Ar}$  suggests that the anisotropy field is rather weak in films to affect the damping. Therefore, spin pumping is the dominant mechanism of enhanced damping observed in W( $p_{Ar}$ )/CoFeB heterostructures and is dependent on the crystallographic structure of the W layer.

The  $\Delta H_0$  signifies the sample quality and is assigned to local dispersions in magnitude and direction of magnetization and anisotropy field. For best sample quality,  $\Delta H_0$  should approach zero. The obtained values of  $\Delta H_0$  are quite small and found to vary between 3 and 8 Oe for W( $p_{Ar}$ )/CoFeB heterostructures [see Fig. 5(c)], indicating very good sample quality. The dispersion can result from changes in the roughness, but as the roughness slightly increases with an increase in  $p_{Ar}$  it cannot explain the observed opposite trend of  $\Delta H_0$  with  $p_{Ar}$ . However, the finite changes in anisotropy field might also affect  $\Delta H_0$  and the correlation between the two with changing  $p_{Ar}$  is also evident.

It is necessary to determine effective spin mixing conductance ( $g_{eff}^{\uparrow\downarrow}$ ) for characterizing the efficiency of spin current passing through the FM/NM interface. The  $g_{eff}^{\uparrow\downarrow}$  is obtained by studying the evolution of Gilbert damping with thickness of the FM layer. To study the role of different W crystal phases on spin pumping efficiency in terms of  $g_{eff}^{\uparrow\downarrow}$ , we carried out CoFeB thickness ( $t_{CoFeB}$ ) dependence of  $\alpha_{eff}$  in W(10 nm,  $p_{Ar}$ )/CoFeB( $t_{CoFeB}$ ) heterostructures with W deposited at  $p_{Ar} = 3$  and 10 mTorr corresponding to mixed ( $\alpha + \beta$ ) and pure  $\beta$  phase, respectively. The typical result is shown in Fig. 6 and the observed linear dependence of  $\alpha_{eff}$  on  $1/t_{CoFeB}$  for both  $p_{Ar} = 3$  and 10 mTorr indicates an interfacial contribution to damping, which is commonly

expected in spin pumping phenomena. The total damping of the system can be derived as [52,53]

$$\alpha_{\text{eff}} = \alpha_B + \alpha_S/t_{\text{CoFeB}}, \quad (3)$$

where  $\alpha_B$  is the intrinsic Gilbert damping constant of bulk CoFeB and  $\alpha_S$  is the interface/surface contribution to effective damping.

The linear fit to the data in Fig. 6 with Eq. (3) yields the values of  $\alpha_B = 0.00527(\pm 0.00007)[0.00526(\pm 0.00038)]$  and  $\alpha_S = 0.0356(\pm 0.0008) \text{ nm}^{-1} [0.0471(\pm 0.0043) \text{ nm}^{-1}]$  for heterostructures with W deposited at  $p_{\text{Ar}} = 3$  mTorr [10 mTorr]. The  $\alpha_S$  value is quite high for both ( $\alpha + \beta$ ) and  $\beta$  phases of W, which signifies prominent interfacial damping due to spin pumping. The estimated net contribution of spin pumping in  $\beta$ -W is somewhat enhanced compared to ( $\alpha + \beta$ )-W. Next, the interfacial  $g_{\text{eff}}^{\uparrow\downarrow}$  can be estimated from the damping enhancement due to spin pumping (i.e.,  $\Delta\alpha_{\text{SP}} = \alpha_S/t_{\text{CoFeB}}$ ) by the following relation [7,8,54,55]:

$$\Delta\alpha_{\text{SP}} = \alpha_S/t_{\text{CoFeB}} = g\mu_B \frac{g_{\text{eff}}^{\uparrow\downarrow}}{4\pi M_s t_{\text{CoFeB}}} \frac{1}{t_{\text{CoFeB}}}. \quad (4)$$

It is noteworthy that the calculation of  $g_{\text{eff}}^{\uparrow\downarrow}$  also includes the contribution of spin back flow from the NM layer back into the FM layer at the interfaces. Taking the value of  $4\pi M_s$  from the VSM measurement, the analysis of  $\Delta\alpha_{\text{SP}}$  leads to  $g_{\text{eff}}^{\uparrow\downarrow} = 1.77(\pm 0.04) \text{ nm}^{-2} [2.35(\pm 0.2) \text{ nm}^{-2}]$  for heterostructures with W deposited at  $p_{\text{Ar}} = 3$  mTorr [10 mTorr]. This suggests that  $g_{\text{eff}}^{\uparrow\downarrow}$  strongly depends on the crystal phase of W, with  $\beta$ -W showing greater  $g_{\text{eff}}^{\uparrow\downarrow}$ . It is known that NM/FM interface morphology (structure and quality) plays a very important role in determining the efficiency of spin transfer across an interface [56,57]. The interface quality does not seem to differ much for W films deposited at  $p_{\text{Ar}} = 3$  and 10 mTorr as there is very little difference in values of roughness, grain size, density, and inhomogeneity of films and as already discussed their role is uncorrelated to the changes in  $\alpha_{\text{eff}}(p_{\text{Ar}})$ .

However, the different crystal phases of W have different atomic as well as electronic structure at the W/CoFeB interface, which might change the interfacial spin-orbit coupling and thus could account for the different  $g_{\text{eff}}^{\uparrow\downarrow}$  values obtained for various W phases. In a similar context, recently, smaller spin Hall angles have been reported for  $\alpha$ -W and mixed ( $\alpha + \beta$ )-W compared to  $\beta$ -W, suggesting a probable correlation with spin mixing conductance [17,36]. Therefore, it is possible to tune the spin pumping efficiency in W( $p_{\text{Ar}}$ )/CoFeB heterostructures utilizing different phases of W resulting from different sample growth conditions.

In the following section, the intrinsic spin mixing conductance ( $g_{\beta\text{-W}}^{\uparrow\downarrow}$ ) of the  $\beta$ -W/CoFeB interface and spin-diffusion length ( $\lambda_{\text{SD}}$ ) of  $\beta$ -W are estimated by investigating the  $\alpha_{\text{eff}}$  dependence on  $\beta$ -W thickness ( $t_W$ ) in  $\beta$ -W( $t_W$ ,  $p_{\text{Ar}} = 10$  mTorr)/CoFeB(15 nm) heterostructures. As  $g_{\text{eff}}^{\uparrow\downarrow}$  depends on thickness and the nature of the NM layer, the  $g_W^{\uparrow\downarrow}$  should be used to characterize the spin pumping. The  $\lambda_{\text{SD}}$  is one of the crucial parameters for studying spin-dependent transport, and for  $t_W > \lambda_{\text{SD}}$  the more likely flipping of the precessing spin occurs before spin returns to the W/CoFeB interface.

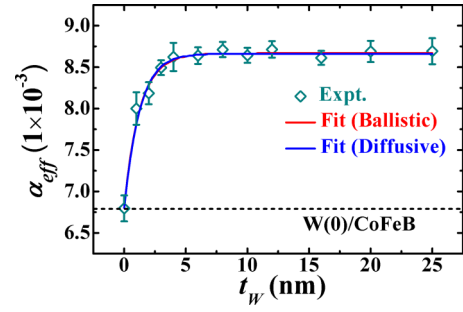


FIG. 7.  $\alpha_{\text{eff}}$  as a function of  $t_W$  for  $\beta$ -W( $t_W$ )/CoFeB(15 nm) heterostructure, with open symbols representing the experimental data and red and blue solid lines being fits to Eqs. (5) and (6), respectively.

The plot of measured  $\alpha_{\text{eff}}$  as a function of  $t_W$  is shown in Fig. 7. With the initial increase of  $\beta$ -W thickness, the  $\alpha_{\text{eff}}$  first increases due to spin pumping in the  $\beta$ -W seed layer and then peaks and remains nearly at a constant level at higher thicknesses. The dependence of  $\alpha_{\text{eff}}$  on  $t_W$  can be described by ballistic and diffusive spin transport models. In the ballistic transport model, the  $\alpha_{\text{eff}}(t_W)$  is fitted with the following simple exponential function [54,58]:

$$\alpha_{\text{eff}} = \alpha_{W(0)/\text{CoFeB}} + g\mu_B \frac{g_{\beta\text{-W}}^{\uparrow\downarrow}}{4\pi M_s t_{\text{CoFeB}}} \frac{1}{t_{\text{CoFeB}}} \left(1 - e^{-\frac{2t_W}{\lambda_{\text{SD}}}}\right), \quad (5)$$

where  $\alpha_{W(0)/\text{CoFeB}}$  is the damping for the CoFeB layer without the W seed layer. The exponential term in the equation refers to the back flow of spin current from the  $\beta$ -W/SiO<sub>2</sub> interface. This back flow of spins adds angular momentum to the CoFeB layer which was previously lost due to spin pumping. The fit to experimental data in Fig. 7 using this model (red line) yields values of  $\lambda_{\text{SD}} = 2.52(\pm 0.18) \text{ nm}$  and  $g_{\beta\text{-W}}^{\uparrow\downarrow} = 1.39(\pm 0.02) \text{ nm}^{-2}$ . The fitted  $\lambda_{\text{SD}}$  is close to the reported values of 3.5 and 2.1 nm [19,59,60]. The fitted value of  $g_{\beta\text{-W}}^{\uparrow\downarrow}$  is smaller than that of the earlier reported W/CoFeB ( $10.1 \text{ nm}^{-2}$ ) [59] system. However, the values are comparable to those reported recently in W/NiFe ( $1.63 \text{ nm}^{-2}$ ) [61] and W/YIG ( $4.5 \text{ nm}^{-2}$ ) systems [60].

In the ballistic model, the resistivity of NM is not considered and the thickness of NM is assumed to be less than the mean free path. In order to include the effect of charge properties of NM on spin transport, the model based on spin-diffusion theory is used to describe  $\alpha_{\text{eff}}(t_W)$  plots. Within this model, the additional damping due to spin pumping is described as [62,63]

$$\Delta\alpha_{\text{SP}} = \alpha_{\text{eff}} - \alpha_{W(0)/\text{CoFeB}} = \frac{g\mu_B}{4\pi M_s t_{\text{CoFeB}}} \frac{g_{\beta\text{-W}}^{\uparrow\downarrow}}{1 + \frac{g_{\beta\text{-W}}^{\uparrow\downarrow}}{g_{\text{ext}}}}, \quad (6)$$

where  $g_{\text{ext}}$  for the NM/FM layer is given by  $g_{\text{ext}} = \frac{h}{e^2 \rho_W \lambda_{\text{SD}}} \tanh\left(\frac{t_W}{\lambda_{\text{SD}}}\right)$ , where  $\rho_W$  is the electrical resistivity of the W layer. The data in the Fig. 7 are nicely fitted using this model (blue line) and the measured resistivity  $\rho_W$  (10 mTorr) =  $447 \mu\Omega \text{ cm}$ . The fit parameters are  $\lambda_{\text{SD}} = 2.34(\pm 0.1) \text{ nm}$  and  $g_{\beta\text{-W}}^{\uparrow\downarrow} = 3.18(\pm 0.24) \text{ nm}^{-2}$ . The value of  $\lambda_{\text{SD}}$  is in good agreement with the ballistic model within the

measurement error and the  $g_{\beta-W}^{\uparrow\downarrow}$  is nearly twice as large as in the ballistic model. Here, the ratio of  $\frac{g_{\beta-W}^{\uparrow\downarrow}}{g_{\text{ext}}^{\uparrow\downarrow}}$  accounts for the back flow of spin current into the pumping FM layer.

The values of  $g_{\text{eff}}^{\uparrow\downarrow}$  extracted from Fig. 6 result from parallel dissipation of spin current into both the W(10 nm) seed layer and Ta(2 nm) cap layer. Thus, the effective spin mixing conductance of the individual W/CoFeB interface, i.e.,  $g_{\text{eff}_W}^{\uparrow\downarrow}$ , could not be determined. For the thickness of W = 10 nm, we can estimate  $g_{\text{eff}_{\beta W}}^{\uparrow\downarrow}$  of the  $\beta$ -W/CoFeB interface from the fitted values of  $g_{\beta-W}^{\uparrow\downarrow}$  using the following two relations corresponding to ballistic and diffusive spin transport:

$$g_{\text{eff}_{\beta W}}^{\uparrow\downarrow} = g_{\beta-W}^{\uparrow\downarrow} \left(1 - e^{-\frac{2t_W}{\lambda_{\text{SD}}}}\right), \quad g_{\text{eff}_{\beta W}}^{\uparrow\downarrow} = \frac{g_{\beta-W}^{\uparrow\downarrow}}{1 + \frac{g_{\beta-W}^{\uparrow\downarrow}}{g_{\text{ext}}^{\uparrow\downarrow}}}. \quad (7)$$

Interestingly, we obtained the same value of  $g_{\text{eff}_{\beta W}}^{\uparrow\downarrow} = 1.39 \text{ nm}^{-2}$  from the two relations, which confirms its validity. The net  $g_{\text{eff}}^{\uparrow\downarrow}$  of the CoFeB layer can be written as the sum of the individual contributions from the W seed layer and Ta cap layer as

$$g_{\text{eff}}^{\uparrow\downarrow} = g_{\text{eff}_W}^{\uparrow\downarrow} + g_{\text{eff}_{\text{Ta}}}^{\uparrow\downarrow}. \quad (8)$$

Using the fit values of  $g_{\text{eff}}^{\uparrow\downarrow}$  (for  $p_{\text{Ar}} = 10 \text{ mTorr}$ ) and  $g_{\text{eff}_{\beta W}}^{\uparrow\downarrow}$ , we calculated the  $g_{\text{eff}_{\text{Ta}}}^{\uparrow\downarrow} = 0.96(\pm 0.2) \text{ nm}^{-2}$ . Since the cap layer structure is the same for all the samples, the  $g_{\text{eff}_{(\alpha+\beta)W}}^{\uparrow\downarrow}$  of the  $(\alpha + \beta)$ -W/CoFeB interface can be similarly calculated and is found to be  $0.81(\pm 0.2) \text{ nm}^{-2}$ .

#### IV. CONCLUSIONS

In summary, we systematically investigated the correlation between argon gas pressure ( $p_{\text{Ar}}$ ) dependent structural phase transition in W thin films and spin pumping efficiency in W/CoFeB heterostructures. X-ray diffraction, XRR, and FMR techniques were used to characterize the crystalline structure, interface, and spin pumping properties of W, which are found to be sensitive with changing  $p_{\text{Ar}}$  in the range 3–20 mTorr. The W films deposited at lower  $p_{\text{Ar}}$  ( $\leq 6 \text{ mTorr}$ ) are dense and smooth with  $(\alpha + \beta)$  phase while higher  $p_{\text{Ar}}$  ( $\geq 10 \text{ mTorr}$ ) forms pure  $\beta$  phase films with reduced density and slightly higher roughness. The stabilization of  $\beta$ -W even at a thickness of 40 nm is associated with increased film porosity and lower deposition flux of W adatoms. In W( $p_{\text{Ar}}$ )/CoFeB heterostructures,  $\beta$ -W leads to more enhancement in magnetic damping ( $\alpha_{\text{eff}}$ ) than  $(\alpha + \beta)$ -W. We observe linear variation in  $\alpha_{\text{eff}}$  with inverse CoFeB thickness for both mixed and pure  $\beta$  phase of W, confirming that spin pumping is the dominant mechanism of damping contribution. The estimated effective spin mixing conductance ( $g_{\text{eff}}^{\uparrow\downarrow}$ ) is found to be larger for  $\beta$ -W compared to  $(\alpha + \beta)$ -W and is attributed to different interface structure which seems to change the interfacial SOC. The observed strong connection of spin pumping efficiency with W crystal phase will allow effective tuning of magnetic damping. Within the framework of ballistic and diffusive spin transport models, the intrinsic spin mixing conductance ( $g_{\beta-W}^{\uparrow\downarrow}$ ) and spin-diffusion length ( $\lambda_{\text{SD}}$ ) of  $\beta$ -W are also calculated by studying the enhancement of  $\alpha_{\text{eff}}$  as a function of  $\beta$ -W thickness. Thus, the results provide insight into developing a complete understanding of the W thin films with high SOC to be subsequently used in spintronics MRAM and spin logic applications.

#### ACKNOWLEDGMENT

D.J. acknowledges the Ministry of Human Resource Development (MHRD), Government of India for providing the senior research fellowship.

- 
- [1] G. A. Prinz, *Phys. Today* **48**, 58 (1995).  
 [2] A. Brataas, Y. V. Nazarov, and G. E. W. Bauer, *Phys. Rev. Lett.* **84**, 2481 (2000).  
 [3] J. E. Hirsch, *Phys. Rev. Lett.* **83**, 1834 (1999).  
 [4] J. Sinova, S.O. Valenzuela, J. Wunderlich, C.H. Back, and T. Jungwirth, *Rev. Mod. Phys.* **87**, 1213 (2015).  
 [5] Y. Tserkovnyak, A. Brataas, and G. E. W. Bauer, *Phys. Rev. B* **66**, 224403 (2002).  
 [6] A. Brataas, Y. Tserkovnyak, G. E. W. Bauer, and B. I. Halperin, *Phys. Rev. B* **66**, 060404 (2002).  
 [7] Y. Tserkovnyak, A. Brataas, G. E. W. Bauer, and B. I. Halperin, *Rev. Mod. Phys.* **77**, 1375 (2005).  
 [8] H. J. Jiao and G. E.W. Bauer, *Phys. Rev. Lett.* **110**, 217602 (2013).  
 [9] G. E.W. Bauer, E. Saitoh, and B. J. Van Wees, *Nature Mater.* **11**, 391 (2012).  
 [10] J. Xiao, G. E.W. Bauer, K. C. Uchida, E. Saitoh, and S. Maekawa, *Phys. Rev. B* **81**, 214418 (2010).  
 [11] Y. Liu, Z. Yuan, R. J. H. Wesselink, A. A. Starikov, and P. J. Kelly, *Phys. Rev. Lett.* **113**, 207202 (2014).  
 [12] H. Ulrichs, V. E. Demidov, S. O. Demokritov, W. L. Lim, J. Melander, N. Ebrahim-Zadeh, and S. Urazhdin, *Appl. Phys. Lett.* **102**, 132402 (2013).  
 [13] Y. Tserkovnyak, A. Brataas, and G. E. W. Bauer, *Phys. Rev. Lett.* **88**, 117601 (2002).  
 [14] A. Brataas, A. D. Kent, and H. Ohno, *Nat. Mater.* **11**, 372 (2012).  
 [15] J. A. Katine and E. E. Fullerton, *J. Magn. Magn. Mater.* **320**, 1217 (2008).  
 [16] T. Jungwirth, J. Wunderlich, and K. Olejník, *Nat. Mater.* **11**, 382 (2012).  
 [17] C.-F. Pai, L. Liu, Y. Li, H. W. Tseng, D. C. Ralph, and R. A. Buhrman, *Appl. Phys. Lett.* **101**, 122404 (2012).  
 [18] C.-F. Pai, M.-H. Nguyen, C. Belvin, L. H. Vilela-Leão, D. C. Ralph, and R. A. Buhrman, *Appl. Phys. Lett.* **104**, 082407 (2014).

- [19] Q. Hao and G. Xiao, *Phys. Rev. Appl.* **3**, 034009 (2015).
- [20] Q. Hao, W. Chen, and G. Xiao, *Appl. Phys. Lett.* **106**, 182403 (2015).
- [21] K.-U. Demasius, T. Phung, W. Zhang, B. P. Hughes, S.-H. Yang, A. Kellock, W. Han, A. Pushp, and S. S.P. Parkin, *Nat. Commun.* **7**, 10644 (2016).
- [22] A. Azevedo, L. H. Vilela-Leão, R. L. Rodríguez-Suárez, A. F. Lacerda Santos, and S. M. Rezende, *Phys. Rev. B* **83**, 144402 (2011).
- [23] K. Ando, S. Takahashi, K. Harii, K. Sasage, J. Ieda, S. Maekawa, and E. Saitoh, *Phys. Rev. Lett.* **101**, 036601 (2008).
- [24] L. Q. Liu, T. Moriyama, D. C. Ralph, and R. A. Buhrman, *Phys. Rev. Lett.* **106**, 036601 (2011).
- [25] L. Liu, C.-F. Pai, Y. Li, H.W. Tseng, D. C. Ralph, and R. A. Buhrman, *Science* **336**, 555 (2012).
- [26] I. M. Miron, K. Garello, G. Gaudin, P.-J. Zermatten, M. V. Costache, S. Auffret, S. Bandiera, B. Rodmacq, A. Schuhl, and P. Gambardella, *Nature (London)* **476**, 189 (2011).
- [27] L. Liu, C.-F. Pai, D. C. Ralph, and R. A. Buhrman, *Phys. Rev. Lett.* **109**, 186602 (2012).
- [28] Z. Duan, A. Smith, L. Yang, B. Youngblood, J. Lindner, V. E. Demidov, S. O. Demokritov, and I. N. Krivorotov, *Nat. Commun.* **5**, 5616 (2014).
- [29] S. Emori, U. Bauer, S.-M. Ahn, E. Martinez, and G. S. D. Beach, *Nature Mater.* **12**, 611 (2013).
- [30] K.-S. Ryu, L. Thomas, S.-H. Yang, and S. Parkin, *Nat. Nanotechnol.* **8**, 527 (2013).
- [31] P. Petroff, T. T. Sheng, A. K. Sinha, G. A. Rozgonyi, and F. B. Alexander, *J. Appl. Phys.* **44**, 2545 (1973).
- [32] Y. G. Shen, Y. W. Mai, Q. C. Zhang, D. R. McKenzie, W. D. McFall, and W. E. McBride, *J. Appl. Phys.* **87**, 177 (2000).
- [33] D. Choi, B. C. Wang, S. Chung, X. Liu, A. Darbal, A. Wise, N. T. Nuhfer, K. Barmak, A. P. Warren, K. R. Coffey, and M. F. Toney, *J. Vac. Sci. Technol. A* **29**, 051512 (2011).
- [34] S. M. Rosnagel, I. C. Noyan, and C. Cabral, *J. Vac. Sci. Technol. B* **20**, 2047 (2002).
- [35] A. J. Narasimham, M. Medikonda, A. Matsubayashi, P. Khare, H. Chong, R. J. Matyi, A. Diebold, and V. P. LaBella, *AIP Adv.* **4**, 117139 (2014).
- [36] S. Mondal, S. Choudhury, N. Jha, A. Ganguly, J. Sinha, and A. Barman, *Phys. Rev. B* **96**, 054414 (2017).
- [37] A. Kumar, R. Bansal, S. Chaudhary, and P. K. Muduli, *Phys. Rev. B* **98**, 104403 (2018).
- [38] D. Jhajhria, D. K. Pandya, and S. Chaudhary, *RSC Adv.* **6**, 94717 (2016).
- [39] A. L. Patterson, *Phys. Rev.* **56**, 978 (1939).
- [40] M. J. O'Keefe and J. T. Grant, *J. Appl. Phys.* **79**, 9134 (1996).
- [41] K. Salamon, O. Milat, N. Radić, P. Dubček, M. Jerčinović, and S. Bernstorff, *J. Phys. D* **46**, 095304 (2013).
- [42] J. A. Thornton, *J. Vac. Sci. Technol.* **11**, 666 (1974).
- [43] C. Kittel, *Phys. Rev.* **73**, 155 (1948).
- [44] B. Cui, C. Song, Y. Y. Wang, W. S. Yan, F. Zeng, and F. Pan, *J. Phys.: Condens. Matter* **25**, 106003 (2013).
- [45] T. Andersen and W. Hübner, *Phys. Rev. B* **74**, 184415 (2006).
- [46] V. Kamberský, *Czech. J. Phys.* **26**, 1366 (1976).
- [47] K. Gilmore, Y. U. Idzerda, and M. D. Stiles, *J. Appl. Phys.* **103**, 07D303 (2008).
- [48] R. Arias, and D. L. Mills, *Phys. Rev. B* **60**, 7395 (1999).
- [49] K. Lenz, H. Wende, W. Kuch, K. Baberschke, K. Nagy, and A. Jánossy, *Phys. Rev. B* **73**, 144424 (2006).
- [50] T. D. Rossing, *J. Appl. Phys.* **34**, 995 (1963).
- [51] D. Jhajhria, D. K. Pandya, and S. Chaudhary, *J. Alloy Compd.* **763**, 728 (2018).
- [52] E. Barati, M. Cinal, D. M. Edwards, and A. Umerski, *Phys. Rev. B: Condens. Matter Mater. Phys.* **90**, 014420 (2014).
- [53] S. Azzawi, A. Ganguly, M. Tokac, R. M. Rowan-Robinson, J. Sinha, A. T. Hindmarch, A. Barman, and D. Atkinson, *Phys. Rev. B: Condens. Matter Mater. Phys.* **93**, 054402 (2016).
- [54] J. M. Shaw, H. T. Nembach, and T. J. Silva, *Phys. Rev. B* **85**, 054412 (2012).
- [55] O. Mosendz, V. Vlaminck, J. E. Pearson, F. Y. Fradin, G. E. W. Bauer, S. D. Bader, and A. Hoffmann, *Phys. Rev. B* **82**, 214403 (2010).
- [56] M. Tokaç, S. A. Bunyaev, G. N. Kakazei, D. S. Schmool, D. Atkinson, and A. T. Hindmarch, *Phys. Rev. Lett.* **115**, 056601 (2015).
- [57] P. Deorani and H. Yang, *Appl. Phys. Lett.* **103**, 232408 (2013).
- [58] J. Foros, G. Woltersdorf, B. Heinrich, and A. Brataas, *J. Appl. Phys.* **97**, 10A714 (2005).
- [59] S. Cho, S. H. C. Baek, K. D. Lee, Y. Jo, and B. G. Park, *Sci. Rep.* **5**, 14668 (2015).
- [60] H. L. Wang, C. H. Du, Y. Pu, R. Adur, P. C. Hammel, and F. Y. Yang, *Phys. Rev. Lett.* **112**, 197201 (2014).
- [61] N. Behera, P. Guha, D.K. Pandya, and S. Chaudhary, *ACS Appl. Mater. Interfaces* **9**, 31005 (2017).
- [62] C. T. Boone, H. T. Nembach, J. M. Shaw, and T. J. Silva, *J. Appl. Phys.* **113**, 153906 (2013).
- [63] C. T. Boone, J. M. Shaw, H. T. Nembach, and T. J. Silva, *J. Appl. Phys.* **117**, 223910 (2015).